Predicting MEG resting-state functional connectivity using microstructural information

Eirini Messaritaki[1,2,3,5], Sonya Foley[1], Simona Schiavi[4], Lorenzo Magazzini[1], Bethany Routley[1], Derek K. Jones[1], and Krish D. Singh[1]

[1]Cardiff University Brain Research Imaging Centre (CUBRIC), School of Psychology, Cardiff University, Maindy Road, Cardiff, CF24 4HQ, UK
[2]BRAIN Biomedical Research Unit, Cardiff University, Maindy Road, Cardiff, CF24 4HQ, UK
[3] Division of Psychological Medicine and Clinical Neurosciences, School of Medicine, Cardiff University, Cardiff, CF24 4HQ, UK
[4] Department of Computer Science, University of Verona, Verona, Italy
[5]Corresponding author. Email: `messaritakie2@cardiff.ac.uk`

Abstract

Understanding the role that human brain microstructure plays in the formation of functional connectivity is an important endeavor that could inform therapies for patients with neurological disorders. In this work, magnetic resonance imaging data from ninety healthy participants were used to perform tractography and calculate structural connectivity matrices, using four microstructural metrics to assign connection strength: number of streamlines, fractional anisotropy, radial diffusivity and a myelin measure (derived from the myelin water fraction computed from multi-component relaxometry). Unweighted binarized structural connectivity matrices, marking with 1 existing structural connections and with 0 non-existing ones, and assigning no specific strength to the connections, were also constructed. Magnetoencephalography resting-state data from the same participants were used to calculate their functional connectivity matrices, via correlations of the Hilbert envelopes of the beamformer time series, at four frequency bands: delta ($1-4$ Hz), theta ($3-8$ Hz), alpha ($8-13$ Hz) and beta ($13-30$ Hz). Non-negative matrix factorization (NMF) was then performed to identify the components of the observed resting-state functional connectivity in those bands. Shortest-path-length and search-information analyses of the structural connectomes were used to predict functional connectivity patterns for both the total resting-state functional connectivity and its NMF components.

The observed functional connectivity was stronger for brain areas that were closer to each other. The microstructurally-informed algorithms predicted the NMF-derived components of the observed functional connectivity more accurately than they predicted the total (non-factorized) observed functional connectivity. The shortest-path-length algorithm outperformed the search-information algorithm in terms of prediction accuracy. When comparing the weights of the structural connectivity matrices, the number of streamlines and the myelin measure gave the most accurate predictions of functional connectivity, while the fractional anisotropy consistently performed poorly. Overall, different structural metrics paint very different pictures of the human structural connectome, of its relationship to functional connectivity, and of which white matter tracts are implicated in the communication between brain areas.

1 Introduction

The representation of the human brain as a network, in which cortical and subcortical areas (nodes) communicate via white matter tracts that carry neuronal signals (connections or edges), has been used extensively to study the brains of healthy people and of patients that suffer from neurological and neuropsychiatric conditions (for example Hagmann et al. (2008); Griffa et al. (2013); Caeyenberghs and Leemans (2014); Fischer et al. (2014); van den Heuvel and Fornito (2014); Yuan et al. (2014); Baker et al. (2015); Collin et al. (2016); Drakesmith et al. (2015b); Aerts et al. (2016); Nelson et al. (2017); Vidaurre et al. (2018); Imms et al. (2019)). Structural networks can be derived from diffusion magnetic resonance imaging (MRI) data via tractography methods (Basser et al., 2000; Mukherjee et al., 2008a,b), and represent the intricate wiring of the human brain that allows communication between different brain areas. Functional networks can be constructed from magnetoencephalography (MEG), electroencephalography (EEG) or functional MRI (fMRI) data, by calculating correlations of brain activity between different brain areas (Biswal et al., 1997; Greicius et al., 2003; Brookes et al., 2011), and represent the possible association of physiological activity in those areas. Comparing structural and functional networks can lead to an understanding of the role of the structural connectome on the evocation of functional connectivity, both in healthy and in diseased brains. It can also shed light into whether, in diseased brains, the local synaptic disruptions and the excitation-inhibition imbalance, and the resulting disrupted functional connectome, lead to structural impairments, or whether it is the structural impairments that lead to functional deficiencies. Such knowledge can inform possible interventions that target structural or functional deficiencies in patients, and therefore can go above and beyond symptom alleviation to improve the brain's performance (Friston et al., 2016).

The effort to relate the human structural and functional connectomes started several years ago. Honey et al. (2009) investigated whether systems-level properties of fMRI-derived functional networks can be accounted for by properties of structural networks, and found that although resting-state functional connectivity (i.e. connectivity in the absence of a task) is frequently present between regions without direct structural connections, its strength, persistence, and spatial patterns are constrained by the large-scale anatomical structure of the human brain. Gõni et al. (2014) used analytic measures of network communication on the structural connectome of the human brain and explored the capacity of these measures to predict resting-state functional connectivity derived from functional MRI data. Shen et al. (2015) showed that resting-state functional connectivity (measured using fMRI) is partly dependent on direct structural connections, but also that dynamic coordination of activity can occur via polysynaptic pathways. Mišić et al. (2016) used singular value decomposition to calculate covariance between the structural and functional (measured with fMRI) connections in data from the Human Connectome Project (Essen et al., 2013), concluding that functional connectivity patterns do not conform to structural connectivity patterns, and that network-wide interactions involve structural connections that do not exist within the functional network in question. Mill et al. (2017) argued that it is essential to consider the temporal variability of resting-state functional connectivity, because that leads to a better understanding of the components that represent task-based connectivity, and therefore of how task-based connectivity can emerge from the structural connectome.

There is also a growing literature on forward generative mechanisms that link microstructure to function (for example Honey et al. (2007, 2009); Deco et al. (2011, 2014, 2017)). Finally, Cabral et al. (2017) give a comprehensive review on the subject.

In this work, we are interested in understanding how the brain microstructure relates to electrophysiological functional connectivity in the human brain. We used MRI and MEG data from ninety healthy participants. Specifically, we used diffusion MRI data to construct their white matter tracts and to derive their structural connectivity networks. Although diffusion MRI is a good method of identifying those tracts, it is insensitive to their myelin content. Given that myelin is believed to play a major role in the formation of functional connectivity in the brain, we also used mcDESPOT data (Deoni et al., 2008) to derive a myelin measure to assign strength to the connections of the structural networks. We used the MEG resting-state recordings to calculate correlations between the electrophysiological activity in different brain areas and derive the resting-state functional connectivity networks of the same participants. We then used the structural networks to predict patterns of functional connectivity based on algorithms proposed by Gõni et al. (2014) and calculated how accurate those predictions are at replicating the observed patterns of the MEG-measured functional connectivity. In order to unravel the richness of the whole-scan connectivity that results from our MEG recordings, we used non-negative matrix factorization to decompose the MEG-measured functional connectivity into fundamental components, and calculated how accurately those components are predicted by the algorithms of Gõni et al. (2014) applied to our structural data. The methodology is described in Sec. 2 and the results are presented in Sec. 3. The implications of our results are discussed in Sec. 4.

2 Methods

All analyses were performed using MATLAB (MATLAB and Statistics Toolbox Release 2015a, The MathWorks, Inc., Massachusetts, United States), unless otherwise stated. An outline of the analysis pipeline is shown in Fig. 1.

2.1 Data acquisition and preprocessing

Ninety healthy participants (58 females, age: $19-34$ years, mean age: 23.7 years, SD: 3.4 years) were scanned at the Cardiff University Brain Research Imaging Centre (CUBRIC), as described in Sec. 2.1.1 and 2.1.2). All participants gave informed consent according to the Declaration of Helsinki and all procedures were approved by the Ethics Committee of the School of Psychology at Cardiff University.

2.1.1 MRI

MRI was carried out on a GE Signa HDx 3T scanner (GE Healthcare, Milwaukee, WI). T1-weighted structural data were acquired using an axial three-dimensional fast spoiled gradient recalled sequence with the following parameters: TR = 8 ms, TE = 3 ms, TI = 450 ms; flip angle = 20°; voxel size = 1 mm; field of view (FOV) ranging from $256 \times 192 \times 160$ mm^3 to $256 \times 256 \times 256$ mm^3 (anterior-posterior / left-right / superior-inferior). The T1 images were downsampled to 1.5 mm isotropic resolution.

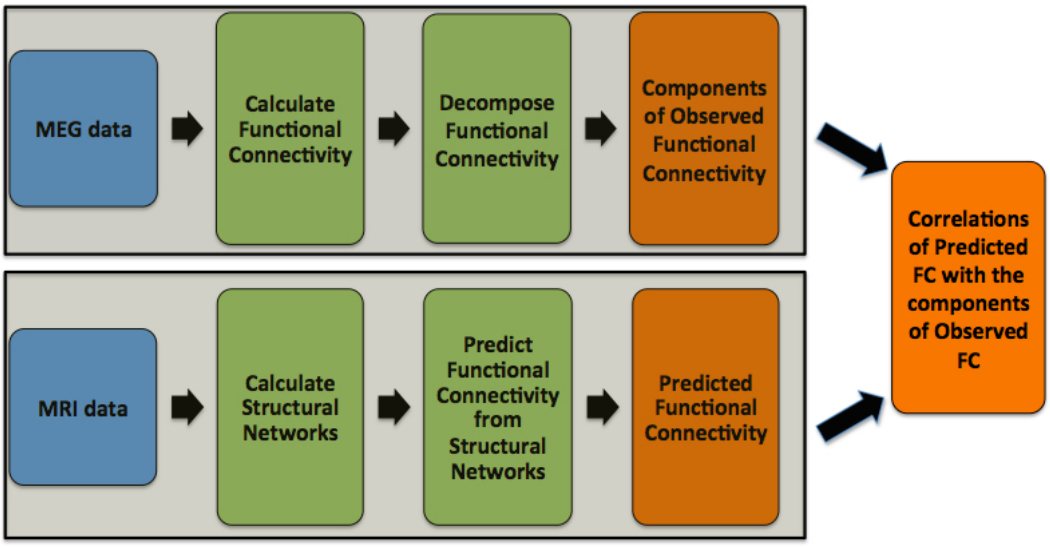

Figure 1: Outline of the methodology.

Diffusion-weighted MRI data were acquired using a peripherally cardiac-gated sequence with b = 1200 s/mm^2, TR = 20 s, TE = 90 ms, isotropic resolution of 2.4 mm, zero slice gap, FOV = 230 mm. Data were acquired along 30 unique and isotropically distributed gradient orientations. Three images with no diffusion weighting were also acquired. The diffusion images were coregistered to the T1-weighted images and corrected for head movement and eddy current distortions. Free-water correction was also performed.

The acquisition and preprocessing of mcDESPOT data (Deoni et al., 2008) was done as described by Zacharopoulos et al. (2017). We briefly describe the method here. The acquisition consisted of spoiled gradient recall (SPGR) images for eight flip angles, one inversion recovery SPGR (IR-SPGR) and steady-state free precession (SSFP) images for eight flip angles and two phase-cycling angles. Twenty-five images were acquired for each participant. All images were acquired in sagittal orientation with a slice matrix of 128×128(1.72×1.72 mm resolution) with a minimum of 88 slices (slice thickness = 1.7 mm). Additional slices were acquired for some participants, in order to ensure full head coverage. The parameters used for each sequence were: SPGR: TE = 2.112 ms, TR = 4.7 ms, flip angles = 3°, 4°, 5°, 6°, 7°, 9°, 13° and 18°. IR-SPGR: TE = 2.112 ms, TR = 4.7 ms, IR = 450 ms, flipangle = 5°. SSFP: TE = 1.6 ms, TR = 3.2 ms, flip angles of 10.59°, 14.12°, 18.53°, 23.82°, 29.12°, 35.29°, 45° and 60°, and phase-cycling angles of 0° and 180°. All images were linearly coregistered to the 13° SPGR image to correct for subject motion. Non-brain tissue was removed using a mask computed with the BET algorithm (Smith et al., 2002). Registration and brain masking were performed with FSL (`http://www.fmrib.ox.ac.uk/fsl/`). The images were then corrected for B1 inhomogeneities and off-resonance artifacts, using maps generated from the IR-SPGR and 2 phase-cycling SSFP acquisitions, respectively. The 3-pool mcDESPOT algorithm was then used to identify the fast (water constrained by myelin) and slow (free-moving water in intra- and extra-

cellular space) components of the T1 and T2 times, and a non-exchanging free-water component (Deoni et al., 2013). The fast volume fraction was taken as a map of the myelin water fraction. The myelin volume fraction was calculated as the ratio of myelin-bound water to total water.

2.1.2 MEG

Five-minute whole-head MEG recordings were acquired in a 275-channel CTF radial gradiometer system, at a sampling rate of 1200 Hz. Twenty-nine additional reference channels were recorded for noise cancellation purposes and the primary sensors were analysed as synthetic third-order gradiometers (Vrba and Robinson, 2001). Participants were seated upright in a magnetically shielded room with their head supported with a chin rest to minimise movement. They were asked to rest with their eyes open and to fixate on a central red point, presented on either a CRT monitor or LCD projector. Horizontal and vertical electro-oculograms (EOG) were recorded to monitor eye blinks and eye movements. Recordings were also acquired while the participants performed tasks after the completion of the resting-state recording, but those recordings were not used in the analysis presented here. To achieve MRI/MEG co-registration, fiduciary markers were placed at fixed distances from three anatomical landmarks identifiable in the participant's T1-weighted anatomical MRI scan, and their locations were manually marked in the MR image. Head localization was performed at the start and end of the MEG recording. The data were subsequently preprocessed in a manner identical to that described in Koelewijn et al. (2019). Specifically, all datasets were down-sampled to 600 Hz, and filtered with a 1 Hz high-pass and a 150 Hz low-pass filter. The datasets were then segmented into 2s epochs, and were visually inspected. Epochs exhibiting large head movements, muscle contractions, or ocular artefacts were excluded from subsequent analysis.

2.2 Network construction

2.2.1 Node definition

The Automated Anatomical Labeling (AAL) atlas (Tzourio-Mazoyer et al., 2002) was used to define, for each participant, the 90 cortical and subcortical areas of the cerebrum that correspond to the nodes of the structural and functional networks. Matching between the cortical and subcortical areas of each participant and the AAL atlas was performed in ExploreDTI-4.6.8 (Leemans et al., 2009). Each network can be represented as a 90×90 symmetric matrix, with each entry indicating the strength of the connection (structural or functional) between the respective nodes. Diagonal elements of those matrices, i.e. self-connections, were set to zero.

2.2.2 Construction of structural networks

The white matter (WM) tracts linking the brain areas are the connections, or edges, of the structural networks. The first step in the construction of the structural networks was to perform tractography using a deterministic streamline algorithm in MRtrix 3.0 (Tournier et al., 2019) (function `tckgen SD_stream`). WM tracts were seeded in the white matter, using a WM mask generated from the T1-weighted images using `FSL fast` (Smith et al., 2004; Jenkinson et al.,

2012). The response function was calculated with spherical harmonic order $l_{\max} = 6$. The maximum allowed angle between successive steps was 45°, and the minimum and maximum tract lengths were 30 and 250 mm respectively. The algorithm was set to select 2×10^5 streamlines. In the subsequent analysis we excluded any tracts that were generated with 5 or fewer streamlines.

The tractograms generated were subsequently used to identify the structural connectomes of the participants, using the MRtrix function `tck2connectome`. Three structural networks were derived to represent the structural connectome for each participant. The edges of those networks were weighted by the number of streamlines scaled by the volume of the two connected nodes (NS), the mean fractional anisotropy (FA) along the streamlines (which has been shown to be correlated with myelination (de Santis et al., 2014), in single-tract voxels), and the mean radial diffusivity (RD) of the streamlines (which has been shown to correlate with axonal diameter by Barazany et al. (2009)). The `tcksample` function was again used to scan the myelin volume fraction (MVF) images and assign the proportion of the MVF that each streamline is responsible for. Then, for each tract, the average myelin measure (MM) along its streamlines was defined to be its edge weight, in order to create a fourth structural network for each participant (MM-weighted). These matrices that resulted from these four edge-weightings were normalized by dividing by the largest value of each matrix, so that, within any given matrix, the values range from 0 to 1. In order to assess the predictive capability of combinations of the WM attributes, we derived data-driven combinations of them based on the method described by Dimitriadis et al. (2017) and used them as edge-weights in the SC matrices used to predict the functional connectivity (FC). Finally, in order to have a measure of the impact of these four edge weightings on our analyses, we also constructed a binarized network for each participant, in which the strength of a structural connection was set to 1 if a WM tract linking the corresponding brain areas existed, and it was set to 0 if such a white matter tract did not exist. We use 'b' to denote those binarized networks.

2.2.3 Construction of functional networks (observed functional connectivity)

The functional networks were constructed in a manner similar to that described by Koelewijn et al. (2019). Specifically, the MEG sensor data were source-localised using FieldTrip (`RRID: SCR_004849`) version 20161011 (Oostenveld et al., 2011), with an LCMV beamformer on a 6 mm grid, using a single-shell forward model (Nolte, 2003), where the covariance matrix was constructed in each of four frequency bands: delta ($1-4$ Hz), theta ($3-8$ Hz), alpha ($8-13$ Hz) and beta ($13-30$ Hz). For each band, the beamformer weights were normalized using a vector norm (Hillebrand et al., 2012), data were normalized to the MNI template, and mapped to 90 nodes based on the Automatic Anatomical Labelling (AAL) atlas (Tzourio-Mazoyer et al., 2002). Epochs were concatenated to generate a continuous virtual-sensor timecourse for each voxel and then band-passed into the above-mentioned frequency bands. For each of the 90 AAL regions, the virtual channel with the greatest temporal standard deviation was selected as the representative one.

The resulting 90 time series were orthogonalized in order to avoid spurious correlations, using symmetric orthogonalization (Colclough et al., 2015). A Hilbert transform was then used to obtain the oscillatory amplitude envelope. The data were subsequently despiked using a median filter in order to remove artefactual temporal transients, downsampled to 1 Hz, and

trimmed to avoid edge effects (removing the first two and the last three samples). Amplitude correlations were calculated by correlating the 90 downsampled Hilbert envelopes to each other, and were converted to variance-normalized z-scores by applying a Fisher transform. This choice was motivated by the fact that such correlations have been shown to be one of the most robust and repeatable electrophysiological connectivity measures (Colclough et al., 2016). We adjusted each participant's functional connectivity matrix to correct for global session effects (Siems et al., 2016). These effects can be generated by experimental session confounds such as head size, head motion and position within the MEG helmet. Such correction procedures are common in fMRI analyses, although there is still debate about what is the optimum algorithm for post-hoc standardization (Yan et al., 2013). In this work we adopted a variant of z-scoring, in which the null mean and standard deviation of connectivity is estimated by fitting a Gaussian (Lowe et al., 1998) to the noise peak ($\pm$ 1 standard deviation) of the distribution. This estimated mean and standard deviation were then used to z-score each Fisher's z connectivity value for that participant. Finally, the weakest values were removed.

Functional connectivity derived from fMRI data has been shown to be impacted by the Euclidean distance between brain areas. In order to assess whether that is the case in our data, the Euclidean distance was plotted against the functional connectivity strength.

2.3 Decomposition of observed functional connectivity

2.3.1 Non-negative matrix factorization

The whole-scan MEG resting-state functional connectivity calculated as described in Sec. 2.2.3 is complex, and could potentially be broken up into fundamental components. Non-negative matrix factorization (NMF) (Lee and Seun, 1999) is a mathematical method that allows a set of matrices to be decomposed into their fundamental components. It has been previously used in MEG studies to decompose time-dependent FC into its fundamental components (Phalen et al., 2019), and allowed for differences between Schizophrenia patients and healthy controls to be quantified. In this work, NMF was used to derive the components that comprise the observed FC (FC_o) for the group of participants, and to identify the contribution that each component has on the whole-scan connectivity of each participant. In NMF, the number of components for the decomposition needs to be specified a-priori, and the resulting components depend on that pre-specified number. This needs to be done with care: a small number of components can result in some details of the FC_o not being captured, while a large number of components can result in at least some of the components being relevant to only a very small number of participants of the group. In our analysis, the number of components was chosen to be the maximum number for which all components were present in at least half of the total number of participants, with a contribution that is at least 5% of the maximum contribution, ensuring that the component is important in explaining the whole-scan FC_o of those participants. The NMF analysis was performed for each frequency band independently, and there was no requirement for the number of components to be identical for the four frequency bands.

As a result of the NMF decomposition, the FC_o of each participant (index i) for the frequency

band f can be written as a sum of the N_f components FC_j, namely:

$$\mathrm{FC}_{\mathrm{o}}^{i} = \sum_{j=1}^{\mathrm{N}_f} a_j^i \times \mathrm{FC}_j. \tag{2.1}$$

The coefficients a_j^i are specific to each participant for each frequency band, while the components FC_j are frequency-band specific.

2.3.2 Calculation of the predicted functional connectivity from the structural connectome

Various algorithms can be used to predict the FC given a substrate of structural connections between the cortical and subcortical areas. A number of such algorithms were described by Gõni et al. (2014) and implemented in the Brain Connectivity Toolbox (Rubinov and Sporns, 2010). These algorithms calculate the potential predictors of FC based on a structural connectivity (SC) matrix, using different methods to identify the optimal links between brain areas, and then use regression to generate a predicted FC that best matches the observed FC. They favor structural connections that are stronger, and take into account both direct and indirect connections between brain areas.

In this work, the search-information (SI) and the shortest-path-length (SPL) algorithms were used to predict the FC for each participant using the five different structural edge-weightings described in Sec. 2.2.2. The analysis was performed for each participant and each frequency band independently. The predicted FC was calculated both for the total $\mathrm{FC_o}$, and for each of the components derived through NMF. In order to assess the impact of the structural edge-weightings and the function-predicting algorithms on the predicted FC ($\mathrm{FC_p}$), the Pearson correlations between $\mathrm{FC_p}$ derived with all possible pairs of edge-weightings and algorithms were calculated, at participant-level for the total (pre-NMF) $\mathrm{FC_o}$. Finally, in order to assess the reliability of the predictions derived with the SI and SPL algorithms for our electrophysiologically-measured FC, the correlations between the $\mathrm{FC_o}$ and the $\mathrm{FC_p}$ were calculated, both for the total connectivity (pre-NMF) and for the NMF-derived components. Because we are interested in the reliability with which the functional connections that were realised are predicted, we do not include in this calculation the functional connections that were zero in the connectivity matrices of the participants.

3 Results

3.1 Observed functional connectivity

The strength of the connections of $\mathrm{FC_o}$ depended on the Euclidean distance between brain areas (Fig. 2), a result that is in agreement with what has been observed for fMRI functional connectivity (for example by Gõni et al. (2014)). There were more and stronger functional connections between brain areas that are directly linked with a WM tract (Fig. 2). However, calculating the mean Euclidean distance between brain areas which are linked with a WM tract and that of those which are not we get the results in Table 1. The distributions of the number of $\mathrm{FC_o}$ connections versus the Euclidean distance for linked and unlinked brain areas is shown in Fig. 3. These

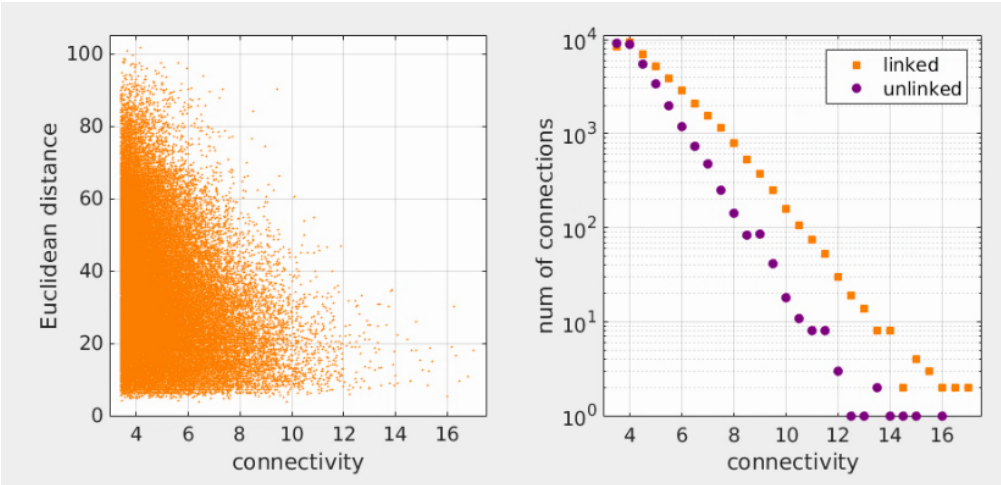

Figure 2: Left: Euclidean distance vs FC_o strength between brain areas. Right: Number of connections vs connection strength, for brain areas that are linked/unlinked with a WM tract.

values are statistically significantly different for each frequency band ($p < 10^{-8}$). The apparent dependence of the strength of functional connectivity on whether or not the brain areas are linked with a WM tract could be due to the fact that, by construction, brain areas that are closer to each other are more likely to have a direct WM tract assigned between them. This implies that it is the Euclidean distance between two brain areas that is the main predictor of the strength of the functional connectivity between them.

Frequency band	Mean Euclidean distance	
	Linked	Unlinked
δ	42.8	53.6
θ	40.1	52.6
α	42.8	53.8
β	42.5	54.4

Table 1: Mean Euclidean distance (mm) between brain areas that exhibit functional connectivity in each frequency band, for areas that are linked with a WM tract, and those that are not linked.

3.1.1 Components of the observed FC

Based on the considerations described in Sec. 2 regarding the number of components in the NMF algorithm, the number of components depended on the frequency band of the FC_o. The maximum number of components for which all components were present for at least half of the participants with a contribution that was at least 5% of the maximum contribution, was 8 for the delta band, 10 for the theta band, 9 for the alpha band and 9 for the beta band. These components

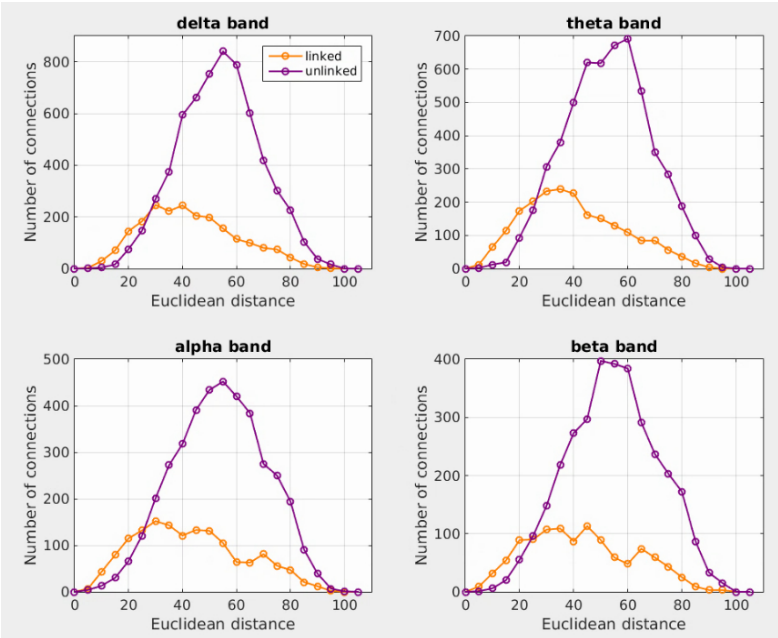

Figure 3: Histogram of the number of FC_o connections versus the Euclidean distance (in mm) for brain areas that are linked or unlinked with a WM tract, for each frequency band.

are shown in Fig. 4, where the strongest 5% of the connections for each FC component are shown. The contribution of the connectivity of each participant to each component is shown in Appendix A.

Most of the components of the FC_o in the delta band exhibit strong frontal connections, except components 2 and 6 which exhibited mostly occipital and well as some parietal connections (Fig. 4). The theta band FC_o was characterized by components with either strong frontal or strong occipital connections. However, components 2 and 3 predominantly had fronto-parietal and fronto-occipital connections respectively (Fig. 4). Most components of the FC_o in the alpha band were dominated by occipital or parietal connections, with the exception of component 3 which predominantly exhibited fronto-parietal connections (Fig. 4). The components of the FC_o in the beta band behaved similarly, but it is noteworthy that components 7 and 8 showed fronto-parietal and temporo-parietal connections separately for the left and right hemispheres (Fig. 4).

3.2 Predicted FC

Fig. 5 shows the SC matrices used in the function-predicting algorithms for one representative participant. Each edge-weighting results in a distinct pattern of SC strength for the structural connections. Of these edge-weightings, the ones that resulted in SC matrices that are correlated were NS-MM (mean of correlations over participants 0.79) and FA-RD (mean of correlations over participants -0.65).

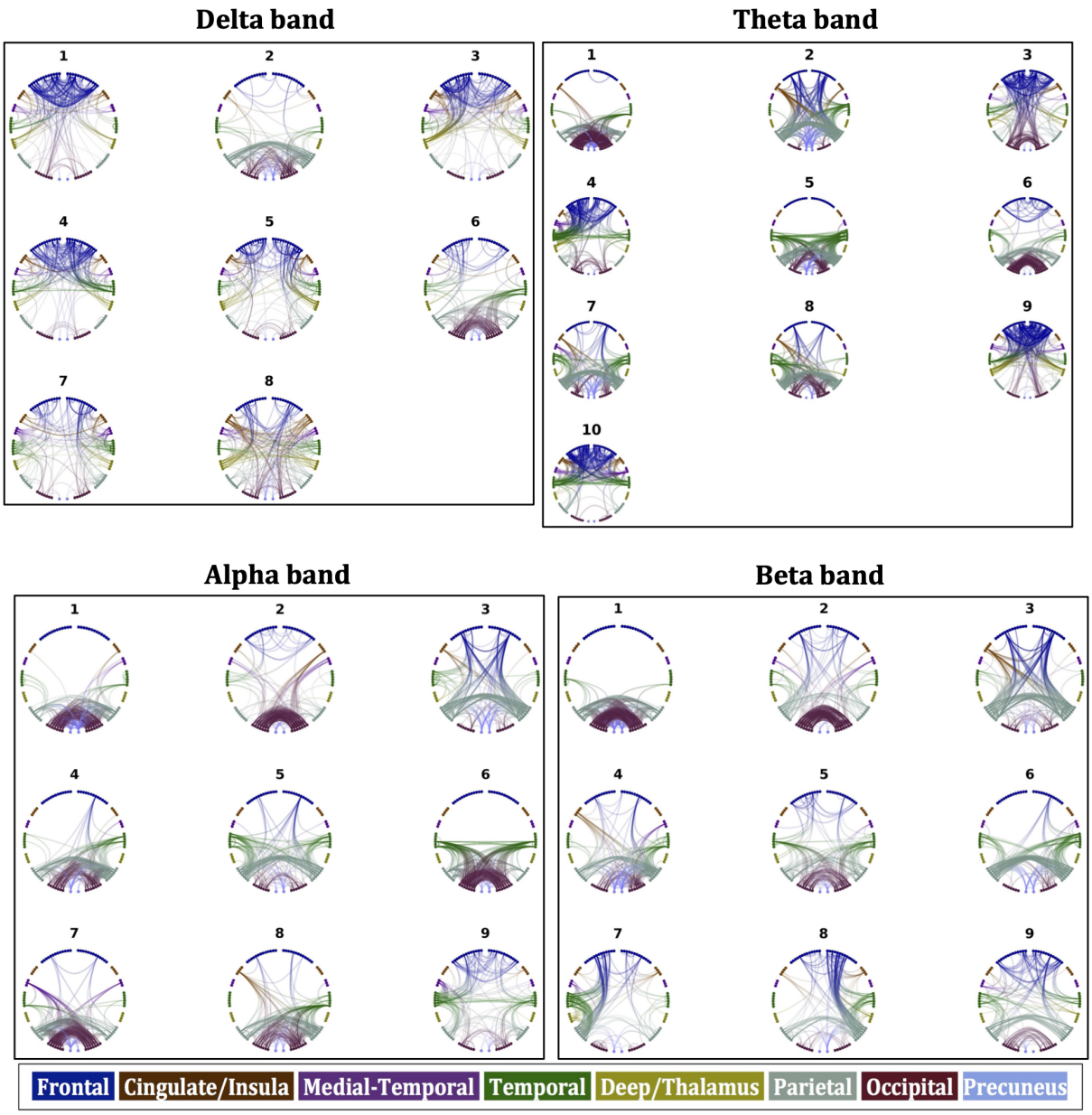

Figure 4: Components of FC_o for the four frequency bands.

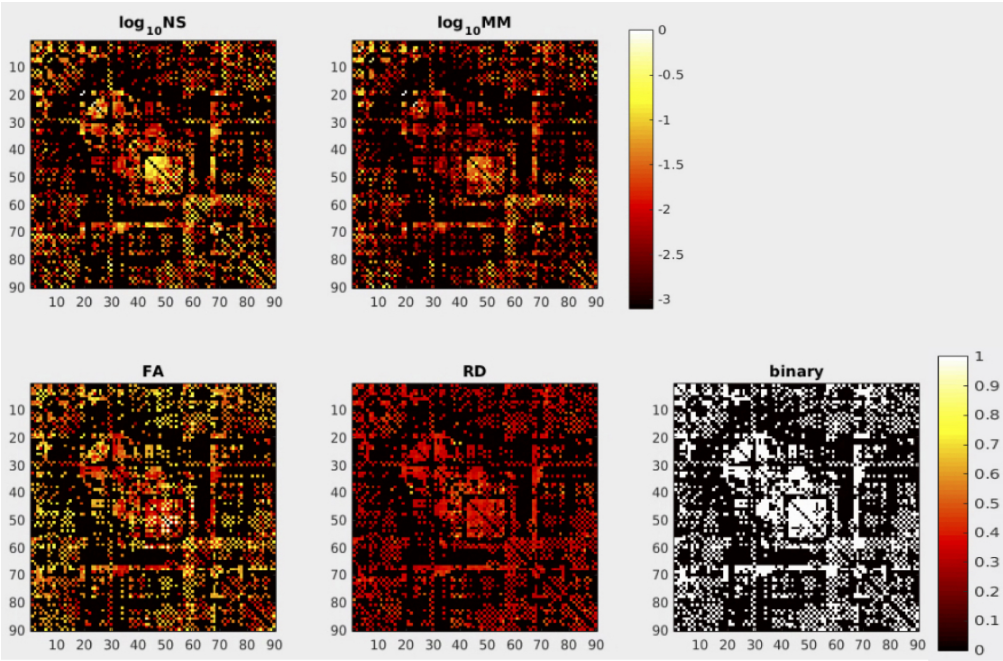

Figure 5: SC matrices for the five different edge-weightings, for one participant. In order to demonstrate the detail of the differences for the NS and MM matrices, we plot the $\log_{10}$ of those metrics.

The patterns of FC_p derived using the different edge-weightings for the structural networks of the participants, and the two FC-predicting algorithms, exhibited high correlations, all with a mean value of above 0.75 (Fig. 6). However, for some participants and some edge-weightings and algorithms the correlations between the FC_p were lower, with values that sometimes go below 0.6. It is noteworthy that the correlations were highest for the delta band, regardless of the pair of algorithm/metric used. We note that the composite structural connectomes that were derived with the algorithm of Dimitriadis et al. (2017) did not provide any improvement in the correlations between structure and function compared to the single-metric structural connectomes, possibly because the true relationship is more complex than that implied by the linear data-driven algorithm. For that reason we do not discuss them any further.

3.3 Correlations between predicted and observed FC

For each edge-weighting, the mean of the distributions (over participants) of the correlations between FC_o and FC_p derived with the SPL algorithm was higher than when derived with the SI algorithm. For that reason, the rest of the paper focuses on FC_p derived using the SPL algorithm. The mean of the distributions for the total FC_o and its components for the 5 SC edge-weightings and the SPL algorithm are shown in Fig. 7. For all five edge-weightings, the correlations for the individual components were higher than the correlations for the total functional connectivity, the only exceptions being two components of the theta band negative connectivity and one component of the beta band negative connectivity.

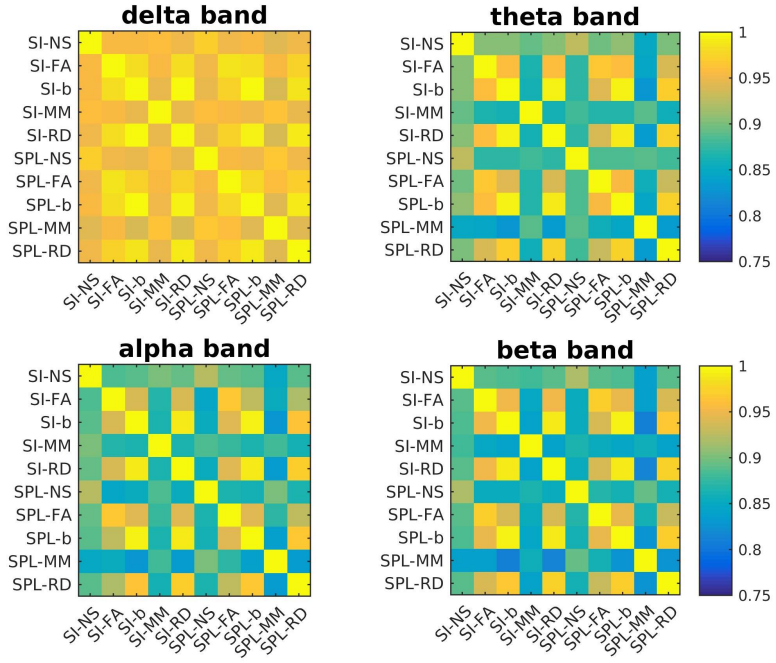

Figure 6: Mean of the correlations of FC_p over participants, with different combinations of structural edge-weightings and function-predicting algorithms. SI = search-information, SPL = shortest-path-length.

The NS-weighting and the MM-weighting gave the highest correlations, and the majority of the distributions resulting from different edge-weightings were statistically significantly different from each other. The difference in the mean correlation value for the optimal choice of edge weighting was up to 0.1, a 33% increase, in some cases. Interestingly, the binarized graphs performed consistently better than the FA-weighted graphs. The p-values for the comparisons of the distributions resulting from all possible combinations of edge-weightings for each component are shown in Tables 2-5 in Appendix B. These tables also show the p-values that survive multiple comparison correction with the false-discovery-rate (FDR) algorithm (Benjamini and Yekutieli, 2001) in bold letters.

3.4 Shortest path length

The length of the shortest path (calculated from the weighted structural connectomes of each participant) for functionally connected brain areas depended on the metric used to weigh the edges of the SC matrices (Fig. 8). Weighting the SC matrices by NS or MM, which gave the highest correlations between FC_o and FC_p, resulted in longer shortest-paths, compared to weighting them by FA or RD or using binarized graphs. With the NS- or MM-weightings, most shortest paths were 2 or 3 steps long, while for the other 3 edge-weightings they were 1 or 2 steps long.

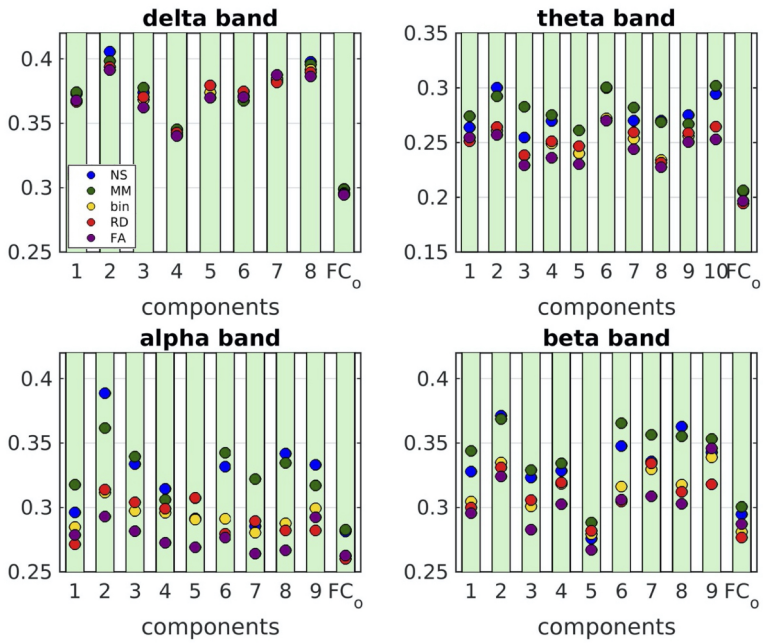

Figure 7: Mean values of the correlations between FC_p and FC_o, for each NMF component and for the total FC_o for all pairs of the 5 structural edge-weightings and SPL algorithms. For clarity of the plots, the plot for the theta band values has a different scale on the y-axis compared to the other three.

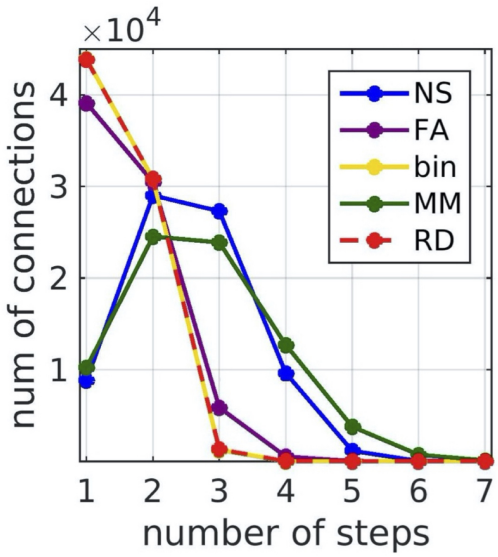

Figure 8: Histogram of the length of the shortest path between functionally connected brain areas, expressed as number of steps calculated based on the structural connectome, for the 5 different structural edge-weightings.

4 Discussion

Our work combines microstructural and electrophysiological brain imaging data to understand the relationship between brain structure and function in the human brain.

4.1 Novel contributions

The novel contributions of the work are as follows:

1. For each participant, we derived structural brain networks for which the edges are weighted with different attributes of the WM tracts that could influence functional connectivity, and binarized networks that only encode whether a structural connection exists or not. We used those structural networks in the search-information and the shortest-path-length algorithms (Gõni et al., 2014) to predict patterns of MEG resting-state functional connectivity, and we compared the resulting patterns. To the best of our knowledge, this is the first time that attributes of WM tracts beyond the number of streamlines and the mean fractional anisotropy are used in such algorithms, and the resulting patterns are compared. It is also the first time that these algorithms are used to predict MEG resting-state functional connectivity.

2. We applied, for the first time, NMF to the whole-scan MEG resting-state FC_o, and identified the components that comprise that FC_o.

3. We used the SI and SPL algorithms of Gõni et al. (2014) to calculate the FC_p both for the total FC_o and for each of its NMF components. We also calculated the correlations between the FC_o and the FC_p, for the total observed functional connectivity and for each of its NMF components. This was done for each of the 5 different edge-weightings in the SC matrices. It reflects the reliability of the function predicting algorithms, and allows us to assess how accurate the different edge-weightings and function-prediction algorithms are at predicting patterns of FC that form the fundamental parts of the whole-scan resting-state MEG FC_o. It also allows us to quantify the impact of the choice of structural edge-weighting and algorithm on the accuracy of the predictions.

4. Motivated by the fact that the SPL algorithm was the best at predicting patterns of MEG resting-state functional connectivity, we used the dMRI-derived structural connectome of each participant to calculate the shortest paths for each connection of the FC_o, for all 5 structural egde-weightings.

4.2 Implications

4.2.1 Implications for the predicted FC

The FC patterns predicted for a given participant, using different structural edge-weightings and algorithms, are similar to each other (Fig. 6), but there are exceptions where those patterns are not well correlated. This indicates that the choice of edge-weighting and algorithm has an impact on the FC_p and consequently on conclusions drawn from such studies. Our analysis also provides a quantification of the impact of the discrepancies that arise when calculating the FC_p with different structural edge-weightings, by calculating the correlations between FC_p and FC_o. The distributions of correlations between FC_p and FC_o were statistically significantly different,

and there is a significant improvement when either the NS or the MM is used to weight the edges of the structural networks. We also showed that for a given structural edge-weighting, the SPL algorithm resulted in higher correlation between the components of FC_p and the FC_o compared to the SI algorithm.

4.2.2 Implications for the observed FC

Brain areas that are close to each other and which are directly linked with a WM tract appeared to have stronger FC_o. However, further analysis of the relationship between the distance of brain areas and whether or not they are linked or not revealed that it is the Euclidean distance that is the dominant predictor. The dependence of the strength of functional connectivity on whether brain areas are directly linked or not appears to be a result of the fact that areas that are closer together are more likely to have a WM tract directly connecting them. This would happen regardless of which brain atlas is used for parcellation.

Decomposing the FC_o using NMF revealed the components that form the complex pattern of the whole-scan FC_o. We now discuss each frequency band separately.

a) Delta band: The FC_o decomposed into components that have strong frontal connections and components that have strong occipital and parietal connections. There is also a separation of left-dominated from right-dominated activation. There is little variation in the mean of the correlations for different structural metrics and algorithms, for each of the 8 components of the FC_o, and even less for the total FC_o. All FC_o components exhibit higher correlations with the FC_p than the total FC_o exhibits with the FC_p.

b) Theta band: The FC_o decomposed into components that are dominated by frontal and parietal interhemispheric connections, as well as fronto-parietal connections. There is little variation in the mean value of the correlations for the total FC_o, however for most of the components of FC_o that value depends strongly on the edge-weighting used. The distributions over participants were statistically significantly different (corrected for multiple comparisons). For components 2 and 9, the NS-weighted SC resulted in the highest correlations, while for the rest the MM-weighting performed the best.

c) Alpha band: The FC_o decomposed into components that have predominantly interhemispheric occipital and parietal connections, as well as fronto-parietal connections (component 3) and temporo-occipital connections (component 6). The mean value of the correlations between the components of FC_o and FC_p was strongly dependent on the edge-weighting used. The corresponding distributions were statistically significantly different for all but a few of the pairs of SC metrics (Table 4 in Appendix B, corrected for multiple comparisons via FDR). The MM and NS were the best predictors of FC_o for most of the components, except component 5. The FA consistently performed poorly compared to those, and also compared to the binarized SC.

d) Beta band: The FC_o decomposed into components that comprise of mainly interhemispheric connections between occipital or parietal areas. There were also intra-hemispheric fronto-parietal and temporo-parietal connections. There was a separation of left- and right-dominated connectivity in the 7th and 8th component. The mean value of the correlations between the components of FC_o and FC_p was strongly dependent on the edge-weighting used, with the corresponding distributions being statistically significantly different (corrected for multiple comparisons) for most the pairs of SC metrics (Table 5 in Appendix B). The MM and NS

were, again, the best predictors of FC_o for most of the components, while the FA consistently performed poorly.

Overall, the NS and MM edge-weightings were better predictors of the FC_o than the FA, which is frequently used in structural network analyses. In fact, the binarized SC matrices performed better than the FA-weighted ones in most cases. This finding, along with the fact that the FA has been shown to exhibit poor repeatability as an edge-weighting in other datasets (Messaritaki et al. (2019a),Messaritaki et al. (2019b)) suggest that the FA is of limited relevance when quantifying structural connectivity and trying to relate it to functional connectivity.

The correlations between the FC_p and the FC_o, both for their non-decomposed values and for the components, were highly variable. For most of the components they were higher than the correlations that the total FC_o exhibited with the FC_p. This indicates that the simplicity of the function-predicting algorithms that we considered is very good at capturing the dynamics of the fundamental components of the FC_o, but perhaps less appropriate for understanding the whole-scan FC_o. The correlations we observed are comparable to the correlations that were reported by Gõni et al. (2014), when they compared structural networks to fMRI-derived functional networks, even though they used average connectomes for the participants involved in their study.

Although our analysis used resting-state data, the documented correspondence between resting-state networks and task-related networks (Smith et al., 2009) indicates that the fundamental organization of the human brain is relatively similar across task and resting-state conditions. The validity of our conclusions should be explored for task-related studies too.

4.3 Assessment of our analysis

Head movement in the MEG system can have a detrimental effect on the measurement of resting-state brain activity, at both beam-former and network level, (Stolk et al., 2013; Messaritaki et al., 2017). To eliminate this confound, the method described by Stolk et al. (2013) and by Messaritaki et al. (2017) would have to be implemented. For that to be possible, continuous head localization throughout the MEG scan is necessary, so that the location of the fiducial points is recorded with the same frequency as the neuronal signals are recorded. However, this information was not recorded during the acquisition of the data. Despite that, the results of Messaritaki et al. (2017) show that the effect of head movement on MEG resting-state functional networks derived via an independent component analysis is small, indicating that the results are robust for head movement that is relatively low.

In our analysis, we considered one measure of MEG-derived functional connectivity, namely correlations between the Hilbert envelopes of the MEG beamformer in different brain areas. Our choice was motivated by the robustness of that measure (Colclough et al., 2016). Network behavior can also be characterised using phase-amplitude and phase-phase correlations of beamformer time series (Siegel et al., 2011), and those should be explored in similar analyses in the future.

Axonal diameter is an important factor when it comes to the formation of brain dynamics (Drakesmith et al., 2019). Including a direct measure of the distributions of axonal diameters in different WM tracts would have been desirable. However, this requires ultra-strong gradients (Veraart et al., 2020) and the data to be acquired with different sequences than those used here. For that reason we used the RD as a possible SC edge-weighting, because it has been shown

to correlate with axon diameter (Barazany et al., 2009). Including such a measure in future analyses could result in more components of the FC_o having higher correlations with the FC_p, as other mechanisms that promote FC are ultimately included in the models.

We only applied a very modest thresholding to the SC matrices. The thresholding of such matrices is an issue of debate nowadays. For example, Buchanan et al. (2020) showed that the spurious WM connections reconstructed with probabilistic tractography can be reduced by different thresholding schemes and give better age associations than if the connections were left unthresholded. On the other hand, Civier et al. (2019) evaluated the removal of weak connections from structural connectomes and concluded that the removal of those connections is inconsequential for graph theoretical analysis, ultimately advocating against the removal of such connections. Finally, Drakesmith et al. (2015a) showed that thresholding can reduce the effects of false positives, but it can introduce its own biases. In our analysis, we used deterministic tractography, which results in fewer false positives (Sarwar et al., 2018). This, along with the fact that the function predicting algorithms we used favor stronger connections, indicate that any further thresholding is unlikely to have a significant impact on the patterns of FC_p.

5 Conclusions

In this study, we used MRI and MEG data to investigate the relationship between brain structure and resting-state functional connectivity in the human brain. Function-predicting algorithms were shown to be good at predicting the building blocks of electrophysiological resting-state functional connectivity, as measured by MEG in our experiment. Different structural edge-weightings resulted in very different pictures for the structural connectome and for its relationship to electrophysiological functional connectivity. The number of streamlines and the myelin measure were the best predictors of the NMF components of the observed functional connectivity, when used with the shortest-path-length algorithm. Our results indicate that the accuracy of the predictions of similar studies can be improved if well-considered structural metrics are used in the analyses.

Acknowledgements

EM was partly funded by the BRAIN Biomedical Research Unit (which is funded by the Welsh Government through Health and Care Research Wales). EM is also funded by a Wellcome Trust ISSF3 Research Fellowship at Cardiff University (204824/Z/16/Z). SF was funded by CUBRIC and the School of Psychology, Cardiff University, and by an ISSF grant to Cardiff University School of Medicine. SS received funding from the University of Verona Internationalisation Programme 2019 (Action 4C). DKJ is funded by a Wellcome Trust Investigator Award (096646/Z/11/Z). DKJ and KDS were supported by a Wellcome Trust Strategic Award (104943/Z/14/Z). The work was also supported by a Wellcome Trust Strategic Award (100202/Z/12/Z), the MRC UK MEG Partnership Grant (MR/K005464/1) and the MRC Doctoral Training Grant (MR/K501086/1). LM and BR were funded by a MRC grant (MR/K005464/1). BR was also funded by MRC grant MR/K501086/1.

Appendices

A Contributions of the components of the observed functional connectivity

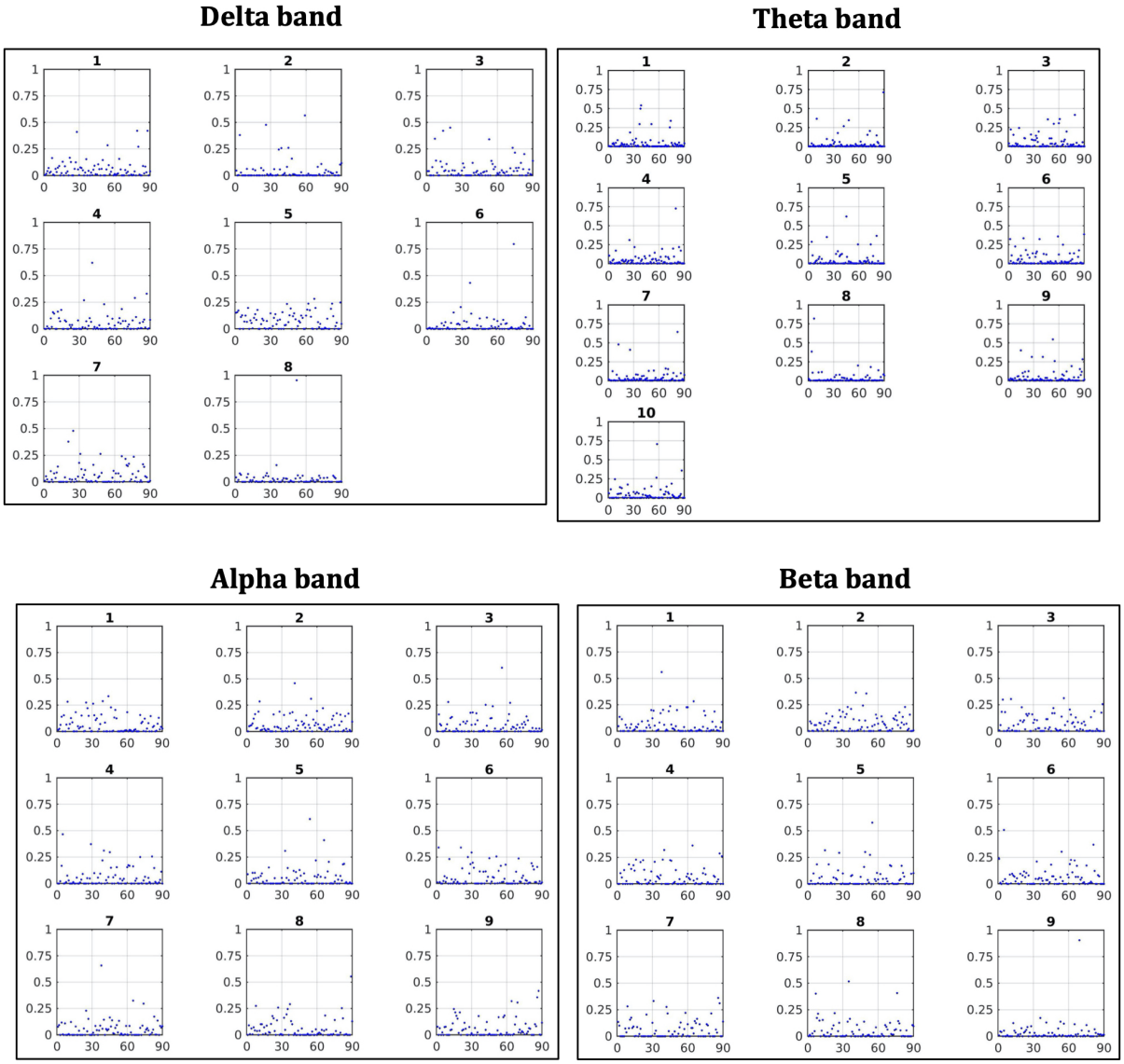

Figure 9: Relative contribution from each participant to each component of the FC_o, for the four frequency bands. The horizontal axis is over the 90 participants.

B Comparison of the correlation distributions

The *p*-values in bold font indicate, for each FC_o component, the pairs of SC edge weightings for which the distributions were *not* statistically significantly different. The multiple comparison correction was performed with FDR over all components and edge-weightings for each frequency band.

Components	SC edge weightings									
	NS-FA	NS-bin	NS-MM	NS-RD	FA-bin	FA-MM	FA-RD	bin-MM	bin-RD	MM-RD
1	4e-04	8e-08	5e-05	2e-07	2e-18	**0.253**	1e-11	7e-15	**0.302**	2e-11
2	2e-08	4e-08	3e-06	8e-08	**0.348**	2e-12	**0.239**	1e-12	6e-03	6e-12
3	**0.344**	1e-09	0.014	6e-07	2e-14	7e-03	3e-08	5e-10	**0.384**	3e-08
4	9e-11	2e-03	**0.082**	0.022	3e-09	4e-06	3e-05	**0.368**	**0.804**	**0.404**
5	5e-07	0.013	2e-08	8e-04	5e-15	**0.281**	8e-14	3e-12	**0.0467**	2e-12
6	4e-11	8e-05	5e-07	4e-06	3e-14	1e-10	3e-08	**0.196**	3e-03	**0.304**
7	6e-07	6e-13	1e-04	1e-13	3e-17	4e-05	5e-17	2e-15	2e-03	2e-15
8	7e-04	0.017	0.015	1e-03	3e-07	0.018	2e-07	3e-05	0.014	6e-06
FC_o	**0.059**	**0.182**	**0.866**	**0.114**	**0.339**	**0.063**	**0.669**	**0.241**	**0.410**	**0.172**

Table 2: Delta band.

Components	SC edge weightings									
	NS-FA	NS-bin	NS-MM	NS-RD	FA-bin	FA-MM	FA-RD	bin-MM	bin-RD	MM-RD
1	8e-14	1e-10	6e-08	9e-11	5e-15	5e-14	3e-09	7e-07	**0.1**	6e-07
2	9e-09	3e-08	2e-12	3e-07	0.013	3e-15	**0.200**	4e-15	**0.851**	2e-14
3	2e-07	1e-04	1e-09	7e-05	8e-04	5e-03	**0.065**	2e-06	**0.262**	6e-04
4	1e-04	2e-09	**0.838**	1e-10	1e-06	3e-05	1e-06	5e-09	0.017	1e-09
5	8e-07	1e-05	5e-10	1e-07	8e-04	6e-14	**0.082**	2e-13	1e-05	1e-13
6	5e-14	9e-13	1e-05	7e-13	2e-11	2e-15	8e-04	1e-13	8e-04	1e-12
7	4e-07	2e-05	4e-15	1e-04	0.010	4e-17	**0.208**	2e-16	**0.785**	5e-15
8	5e-04	9e-04	1e-09	0.012	**0.184**	8e-12	**0.049**	4e-12	**0.127**	9e-11
9	**0.103**	5e-06	**0.188**	2e-04	3e-11	**0.878**	2e-09	1e-04	0.009	0.001
10	**0.283**	0.001	**0.046**	0.002	3e-07	**0.372**	2e-06	2e-04	**0.4673**	2e-04
FC_o	**0.0663**	**0.053**	**0.763**	**0.016**	**0.973**	**0.037**	**0.505**	**0.085**	**0.261**	**0.033**

Table 3: Theta band.

Components	SC edge weightings									
	NS-FA	NS-bin	NS-MM	NS-RD	FA-bin	FA-MM	FA-RD	bin-MM	bin-RD	MM-RD
1	2e-19	6e-16	1e-08	4e-16	2e-16	7e-19	6e-05	4e-13	5e-05	1e-13
2	1e-23	2e-15	3e-22	2e-14	8e-26	1e-16	1e-19	11e-09	**0.656**	2e-06
3	2e-09	4e-12	3e-12	3e-11	4e-07	2e-15	2e-05	2e-16	0.015	6e-16
4	3e-10	4e-09	2e-04	7e-09	2e-04	1e-15	**0.187**	3e-15	**0.302**	2e-14
5	4e-07	0.002	2e-11	0.006	4e-05	1e-12	0.002	2e-11	**0.951**	3e-10
6	9e-09	**0.049**	0.021	2e-05	6e-15	5e-14	8e-05	1e-06	6e-08	1e-10
7	8e-12	9e-09	0.041	6e-07	7e-13	3e-15	1e-08	1e-10	**0.284**	1e-07
8	5e-10	2e-08	3e-08	1e-08	9e-07	3e-16	**0.052**	6e-16	**0.081**	1e-15
9	1e-09	0.022	**0.338**	**0.154**	6e-17	3e-11	8e-14	5e-04	**0.052**	0.026
FC_o	3e-05	2e-06	**0.689**	7e-08	**0.847**	6e-10	**0.409**	1e-07	**0.217**	1e-08

Table 4: Alpha band.

Components	SC edge weightings									
	NS-FA	NS-bin	NS-MM	NS-RD	FA-bin	FA-MM	FA-RD	bin-MM	bin-RD	MM-RD
1	2e-16	6e-15	4e-03	9e-15	5e-12	2e-19	1e-04	6e-18	**0.135**	3e-16
2	2e-23	7e-15	2e-23	1e-14	1e-25	2e-12	8e-20	8e-13	**0.067**	1e-08
3	2e-10	6e-16	5e-15	2e-15	2e-14	7e-20	1e-11	1e-21	0.006	1e-21
4	3e-09	1e-06	1e-12	4e-08	3e-07	2e-17	**0.227**	4e-16	7e-04	8e-16
5	8e-10	6e-05	**0.077**	2e-08	3e-11	7e-12	**0.045**	2e-05	1e-09	2e-09
6	6e-04	7e-03	4e-11	4e-03	0.021	5e-12	**0.309**	3e-12	**0.381**	6e-12
7	1e-08	**0.681**	2e-07	4e-03	3e-14	2e-12	3e-09	2e-06	1e-09	1e-09
8	0.022	**0.900**	1e-11	5e-06	1e-04	6e-11	0.005	4e-10	6e-11	3e-13
9	1e-06	6e-04	**0.558**	9e-06	1e-04	7e-09	**0.231**	3e-05	1e-04	8e-07
FC_o	**0.079**	4e-04	**0.098**	6e-06	0.016	9e-05	0.001	7e-07	0.008	1e-08

Table 5: Beta band.

References

H. Aerts, W. Fias, K. Caeyenberghs, and D. Marinazzo. Brain networks under attack: robustness properties and the impact of lesions. *Brain*, 139:3063–3083, 2016.

S.T.E. Baker, D.I. Lubman, M. Yucel, N.B. Allen, S. Whittle, B.D. Fulcher, A. Zalesky, and A. Fornito. Developmental changes in brain network hub connectivity in late adolescence. *Journal of Neuroscience*, 35(24):9078–9087, 2015.

D. Barazany, P.J. Basser, and Y. Assaf. In *vivo* measurement of axon diameter distribution in the corpus callosum of rat brain. *BRAIN*, 132:1210–1220, 2009.

P.J. Basser, S. Pajevic, C. Pierpaoli, J. Duda, and A. Aldroubi. In-vivo fiber tractography using DT-MRI data. *Magnetic Resonance in Medicine*, 44(4):625–632, 2000.

Y. Benjamini and D. Yekutieli. The control of the false discovery rate in mulitple testng under dependency. *The Annals of Statistics*, 29(4):1165–1188, 2001.

B.B. Biswal, J. VanKylen, and J.S. Hyde. Simultaneous assessment of flow and bold signals in resting-state functional connectivity maps. *NMR in Biomedicine*, 10:165–170, 1997.

M.J. Brookes, M. Woolrich, H. Luckhoo, D. Price, J.R. Hale, M. C. Stephenson, G.R. Barnes, S.M. Smith, and P.G. Morris. Investigating the electrophysiological basis of resting state networks using magnetoencephalography. *Proceedings of the National Academy of Sciences of the United States of America*, 2011.

C.R. Buchanan, M.E. Bastin, S.J. Ritchie, D.C. Liewald, J.W. Madole, E.M. Tucker-Drob, I.J. Deary, and S.R. Cox. The effect of network thresholding and weighting on structural brain networks in the UK biobank. *NeuroImage*, In press, 2020.

J. Cabral, M.L. Kringelbach, and G. Deco. Functional connectivity dynamically evolves on multiple time-scales over a static structural connectome: Models and mechanisms. *NeuroImage*, 160:84–96, 2017.

K. Caeyenberghs and A. Leemans. Hemispheric lateralization of topological organization in structural brain networks. *Human Brain Mapping*, 35(9):4944–4957, 2014.

O. Civier, R. Elton Smith, C.-H. Yeh, A. Connelly, and F. Calamante. Is removal of weak connections necessary for graph-theoretical analysis of dense weighted structural connectomes from diffusion MRI? *NeuroImage*, 194: 68–81, 2019.

G.L. Colclough, M.J. Brookes, S.M. Smith, and M.W. Woolrich. A symmetric multivariate leakage correction for MEG connectomes. *NeuroImage*, 117:439–448, 2015.

G.L. Colclough, M.W. Woolrich, P.K. Tewarie, M.J. Brookes, A.J. Quinn, and S.M. Smith. How reliable are meg resting-state connectivity metrics? *NeuroImage*, 138:284–293, 2016.

G. Collin, M.P. van den Heuvel, L. Abramovic, A. Vreeker, M.A. de Reus, N.E.M van Haren, M.P.M. Boks, R.A. Ophoff, and R.S. Kahn. Brain network analysis reveals affected connectome structure in bipolar i disorder. *Human Brain Mapping*, 27:122–134, 2016.

S. de Santis, M. Drakesmith, S. Bells, Y. Assaf, and D.K. Jones. Why diffusion tensor mri does well only some of the time: variance and covariance of white matter tissue microstructure attributes in the living human brain. *NeuroImage*, 89:35–44, 2014.

G. Deco, V.K. Jirsa, and A.R. McIntosh. Emerging concepts for the dynamical organization of resting-state activity in the brain. *Nature Reviews Neuroscience*, 12(1):43, 2011.

G. Deco, A.R. McIntosh, K. Shen, R.M. Hutchinson, R.S. Menon, S. Everling, P. Hagmann, and V.K. Jirsa. Identification of optimal structural connectivity using functional connectivity and neural modelling. *Journal of Neuroscience*, 34(23):7910–7916, 2014.

G. Deco, J. Cabral, M.W. Woolrich, A.B.A. Stevner, T.J. van Hartevelt, and M.L. Kringelbach. Single or multiple frequency generators in on-going brain activity: A mechanistic whole-brain model of empirical MEG data. *NeuroImage*, 152:538–550, 2017.

S. Deoni, L. Matthews, and S. Kolind. One component? Two components? Three? The effect of including a nonexchanging "free" water component in multicomponent driven equilibrium single pulse observation of T1 and T2. *Magnetic Resonance in Medicine*, 70:147–154, 2013.

S.C. Deoni, B.K. Rutt, T. Arun, C. Pierpaoli, and D.K. Jones. Gleaning multi-component T1 and T2 information from steady-state imaging data. *Proceedings of the International Society for Magnetic Resonance in Medicine*, 2008.

S.I. Dimitriadis, M. Drakesmith, S. Bells, G.D. Parker, D.E. Linden, and D.K. Jones. Improving the reliability of network metrics in structural brain networks by integrating different network weighting strategies into a single graph. *Frontiers in Neuroscience*, 11:694, 2017.

M. Drakesmith, K. Caeyenberghs, A. Dutt, G. Lewis, A.S. David, and D.K. Jones. Overcoming the effects of false positives and threshold bias in graph theoretical analysis of neuroimaging data. *NeuroImage*, 118:313–333, 2015a.

M. Drakesmith, K. Caeyenberghs, A. Dutt, S. Zammit, C.J. Evans, A. Reichenberg, G. Lewis, A.S. David, and D.K. Jones. Schizophrenia-like topological changes in the structural connectome of individuals with subclinial psychotic experiences. *Human Brain Mapping*, 36:2629–2643, 2015b.

M. Drakesmith, R. Harms, S.U. Rudrapatna, G.D. Parker, C.J. Evans, and D.K. Jones. Estimating axon conduction velocity in vivo from microstructural MRI. *NeuroImage*, 203:116186, 2019.

D.C. Van Essen, S.M. Smith, D.M. Barch, T.E.J. Behrens, E. Yacoub, and K. Ugurbil for the WU-Minn HCP Consortium. The WU-Minn Human Connectome Project: an overview. *NeuroImage*, 80:62–79, 2013.

F.U. Fischer, D. Wolf, A. Scheurich, and A. Fellgiebel. Association of structural global brain network properties with intelligence in normal aging. *PLoS ONE*, 9(1):e86258, 2014.

K. Friston, H.R. Brown, J. Siemerkus, and K.E. Stephan. The dysconnection hypothesis (2016). *Schizophrenia Research*, 176(2-3):83–94, 2016.

J. Gõni, M. P. van den Heuvel, A. Avena-Koenigsberger, N. Velez de Mendizabal, R. F. Betzel, A. Griffa, P. Hagmann, B. Corominas-Murtra, J.-P. Thiran, and O. Sporns. Resting-brain functional connectivitypredicted by analytic measures of network communication. *Proceedings of the National Academy of Sciences of the United States of America*, 111(2):833–838, 2014.

M.D. Greicius, B. Krasnow, A.L. Reiss, and V. Menon. Functional connectivity in the resting brain: A network analysis of the default mode hypothesis. *Proceedings of the National Academy of Sciences of the United States of America*, 100(1):253–258, 2003.

A. Griffa, P.S. Baumann, J.-P. Thiran, and P. Hagmann. Structural connectomics in brain diseases. *NeuroImage*, 80: 515–526, 2013.

Patric Hagmann, Leila Cammoun, Xavier Gigandet, Reto Meuli, Christopher J Honey, Van J Wedeen, and Olaf Sporns. Mapping the structural core of human cerebral cortex. *PLOS Biology*, 6(7):1–15, 07 2008. doi: 10.1371/journal.pbio.0060159. URL `https://doi.org/10.1371/journal.pbio.0060159`.

A. Hillebrand, G.R. Barnes, J.L. Bosboom, H.W. Berendse, and C.J. Stam. Frequency-dependent functional connectivity within resting-state networks: an atlas-based MEG beamformer solution. *NeuroImage*, 59:3909–3921, 2012.

C.J. Honey, R. Kötter, M. Breakspear, and O. Sporns. Network structure of cerebral cortex shapes functional connectivity on mulitple time scales. *Proceedings of the National Academy of Sciences of the United States of America*, 104(24):10240–10245, 2007.

C.J. Honey, O. Sporns, L. Cammoun, X. Gigandet, J.P. Thiran, R. Meuli, and P. Hagmann. Predicting human resting-state functional connectivity from structural connectivity. *Proceedings of the National Academy of Sciences*, 106: 2035–2040, 2009.

P. Imms, A. Clemente, M. Cook, W. D'Souza, P.H. Wilson, D.K. Jones, and K. Caeyenberghs. The structural connectome in traumatic brain injury: A meta-analysis of graph metrics. *Neuroscience and Behavioural Reviews*, 2019.

M. Jenkinson, C.F. Beckmann, T.E. Behrens, M.W. Woolrich, and S.M. Smith. FSL. *NeuroImage*, 62:782–790, 2012.

L. Koelewijn, T.M. Lancaster, D. Linden, D.C. Dima, B.C. Routley, L. Magazzini, K. Barawi, L. Brindley, R. Adams, K.E. Tansey, A. Bompas, A. Tales, A. Bayer, and K.D. Singh. Oscillatory hyperactivity and hyperconnectivity in young APOE-ε4 carriers and hypoconnectivity in Alzheimer's disease. *eLife*, 8:e36011, 2019.

D.D. Lee and H.S. Seun. Learning the parts of objects by non-negative matrix factorization. *Nature*, 401:788, 1999.

A. Leemans, B. Jeurissen, J. Sijbers, and D.K. Jones. ExploreDTI: a graphical toolbox for processing, analyzing, and visualizing diffusion MRI data. *17th Annual Meeting of the International Society for Magnetic Resonance in Medicine*, Hawaii, USA:3537, 2009.

M.J. Lowe, B.J. Mock, and J.A. Sorenson. Functional connectivity in single and multislice echoplanar imaging using resting-state fluctuations. *NeuroImage*, 7(2):119–132, 1998.

E. Messaritaki, L. Koelewijn, D.C. Dima, G.M. Williams, G. Perry, and K.D. Singh. Assessment and elimination of the effects of head movement of meg resting-state networks of oscillatory brain activity. *NeuroImage*, 159: 302–324, 2017.

E. Messaritaki, S.I. Dimitriadis, and D.K. Jones. Optimization of graph construction can significantly increase the power of structural brain network studies. *NeuroImage*, 199:495–511, 2019a.

E. Messaritaki, S.I. Dimitriadis, and D.K. Jones. Assessment of the reproducibility of structural brain networks derived using different edge-weighting streategies. *Proceedings of the 27th Annual Meeting of the ISMRM, Montreal, Canada*, 2019b.

R.D. Mill, T. Ito, and M.W. Cole. From connectome to cognition: The search for mechanism in human functional brain networks. *NeuroImage*, 160:124–139, 2017.

B. Mišić, R.F. Betzel, M.A. de Reus, M.P. van den Heuvel, M.G. Berman, A.R. McIntosh, and O. Sporns. Network-level structure-function relationships in human neocortex. *Cerebral Cortex*, 26:3285–3296, 2016.

P. Mukherjee, J.I. Berman, S.W. Chung, C.P. Hess, and R.G. Henry. Diffusion tensor MR imaging and fiber tractography: theoretical underpinnings. *Americal Journal of Neuroradiology*, 29(4):632–641, 2008a.

P. Mukherjee, J.I. Berman, S.W. Chung, C.P. Hess, and R.G. Henry. Diffusion tensor MR imaging and fiber tractography: technical considerations. *American Journal of Neuroradiology*, 29(5):843–852, 2008b.

B.G. Nelson, D.S. Bassett, J. Camchong, E.T. Bullmore, and K.O. Lim. Comparison of large-scale human brain function and anatomical networks in schizophrenia. *NeuroImage: Clinical*, 15:439–448, 2017.

G. Nolte. The magnetic lead field theorem in the quasi-static approximation and its use for magnetoencephalography forward calculation in realistic volume conductors. *Physics in Medicine and Biology*, 48:3637–3652, 2003.

R. Oostenveld, P. Fries, E. Maris, and J.M. Scholffelen. Fieldtrip: Open source software for advanced analysis of MEG, EEG and invasive electrophysiological data. *Computational Intelligence and Neuroscience*, 2011:1–9, 2011.

H. Phalen, B.A. Coffman, A. Ghuman, E. Sejdić, and D.F. Salisbury. Non-negative matrix factorization reveals resting-state cortical alpha network abnormalities in the first-episode schizophrenia spectrum. *Biological Psychiatry: Congitive Neuroscience and Neuroimaging*, in press, 2019.

M. Rubinov and O. Sporns. Complex network measures of brain connectivity: Uses and interpretations. *NeuroImage*, 52(3):1059–1069, 2010.

T. Sarwar, K. Ramamohanarao, and A. Zalesky. Mapping connectomes with diffusion MRI: deterministic or probabilistic tractography. *Magnetic Resonance in Medicine*, 81:1368–1384, 2018.

K. Shen, R.M. Hutchison, G. Bezgin, S. Everling, and A.R. McIntosh. Network structure shapes spontaneous functional connectivity dynamics. *The Journal of Neuroscience*, 35(14):5579–5588, 2015.

M. Siegel, T.H. Donner, and A.K. Engel. Spectral fingerprints of large-scale neuronal interactions. *Nature Reviews Neuroscience*, 13:121–134, 2011.

M. Siems, A.-A. Pape, J.F. Hippa, and M. Siegel. Measuring the cortical correlation structure of spontaneous oscillatory activity with EEG and MEG. *NeuroImage*, 129:345–355, 2016.

S.M. Smith, Y. Zhang, M. Jenkinson, J. Chen, P.M. Matthews, A. Federico, and N. De Stefano. Accurate, robust and automated longitudinal and cross-sectional brain change analysis. *NeuroImage*, 17(1):479–489, 2002.

S.M. Smith, M. Jenkinson, M.W. Woolrich, C.F. Beckmann, T.E.J. Behrens, H. Jonansen-Berg, P.R. Bannister, M. De Luca, I. Drobnjak, D.E. Flitney, R. Niazy, J. Saunders, J. Vickers, Y. Zhang, N. De Stefano, J.M. Brady, and P.M. Matthews. Advances in functional and structural MR image analysis and implementation as FSL. *NeuroImage*, 23(S1):208–219, 2004.

S.M. Smith, P.T. Fox, K.L. Miller, D.C. Glahn, P.M. Fox, C.E. Mackay, N. Filippini, K.E. Watkins, R. Toro, and A.R. Lairdand C.F. Beckmann. Correspondence of the brain's functional architecture during activation and rest. *PNAS*, 106:31:13040–13045, 2009.

A. Stolk, A. Todorovic, J.-M. Schoffelen, and R. Oostenveld. Online and offline tools for head movement compensation in MEG. *NeuroImage*, 68:39–48, 2013.

J.-D. Tournier, R.E. Smith, D. Raffelt, R. Tabbara, T. Dhollander, M. Pietsch, D. Christiaens, B. Jeurissen, C.-H. Yeh, and A. Connelly. MRtrix3: A fast, flexible and open software framework for medical image processing and visualisation. *NeuroImage*, 202:116–137, 2019.

N. Tzourio-Mazoyer, B. Landeau, D. Papathanassiou, F. Crivello, O. Etard, N. Delcroix, B. Mazoyer, and M. Joliot. Automated anatomical labeling of activations in SPM using a macroscopic anatomical parcelation of the MNI MRI single-subject brain. *NeuroImage*, 15:273–289, 2002.

M.P. van den Heuvel and A. Fornito. Brain networks in schizophrenia. *Neuropsychology Review*, 24(1):32–48, 2014.

J. Veraart, D. Nunes, U. Rudrapatna, E. Fieremans, D.K. Jones, D.S. Novikov, and N. Shemesh. Nonivasive quantification of axon radii using diffusion MRI. *Elife*, 2020. URL `10.7554/elife.49855`.

D. Vidaurre, R. Abeysuriya, R. Becker, A.J. Quinn, F. Alfaro-Almagro, S.M. Smith, and M.W. Woolrich. Discovering dynamic brain networks from big data in rest and task. *NeuroImage*, 180(B):646–656, 2018.

J. Vrba and S.E. Robinson. Signal processing in magnetoencephalography. *Methods*, 25:249–271, 2001.

C.-G. Yan, R.C. Craddock, X.-N. Zuo, Y.-F. Zang, and M.P. Milham. Standardizing the intrinsic brain: towards robust measurement of inter-individual variation in 1000 functional connectomes. *NeuroImage*, 80:246–262, 2013.

W. Yuan, S.L. Wade, and L. Babcock. Structural connectivity abnormality in children with acute mild traumatic brain injury using graph theoretical analysis. *Human Brain Mapping*, 36:779–792, 2014.

G. Zacharopoulos, P.H.P. Hanel, T.M. Lancaster, N. Ihssen, M. Drakesmith, S. Foley, G.R. Maio, and D.E.J. Linden. Nonlinear associations between human values and neuroanatomy. *Social Neuroscience*, 12:6:673–684, 2017.